

DivAS: Interactive 3D Segmentation of NeRFs via Depth-Weighted Voxel Aggregation

Ayush Pande

IIT Kanpur

ayushp@cse.iitk.ac.in

Abstract

*Existing methods for segmenting Neural Radiance Fields (NeRFs) are often optimization-based, requiring slow per-scene training that sacrifices the zero-shot capabilities of 2D foundation models. We introduce **DivAS** (Depth-interactive Voxel Aggregation Segmentation), an optimization-free, fully interactive framework that addresses these limitations. Our method operates via a fast GUI-based workflow where 2D SAM masks, generated from user point prompts, are refined using NeRF-derived depth priors to improve geometric accuracy and foreground-background separation. The core of our contribution is a custom CUDA kernel that aggregates these refined multi-view masks into a unified 3D voxel grid in under 200ms, enabling real-time visual feedback. This optimization-free design eliminates the need for per-scene training. Experiments on Mip-NeRF 360° and LLFF show that DivAS achieves segmentation quality comparable to optimization-based methods, while being 2–2.5× faster end-to-end, and up to an order of magnitude faster when excluding user prompting time.*

1. Introduction

The ability to efficiently segment and annotate 3D scenes is fundamental to numerous computer vision and graphics applications, ranging from content creation to autonomous perception. Recent years have witnessed remarkable progress in two parallel directions: neural implicit representations for 3D scene modeling and foundation models for large-scale image understanding. This paper explores the convergence of these paradigms through the lens of interactive 3D segmentation with human in the loop.

Neural Radiance Fields (NeRF) [20] have emerged as a powerful implicit representation for 3D scenes, enabling photorealistic rendering from arbitrary viewpoints without requiring explicit geometry extraction. By parameterising a scene as a continuous volumetric function optimised via dif-

ferentiable volume rendering, NeRFs have revolutionized novel view synthesis. Variants such as Mip-NeRF 360° [3] extend this paradigm to unbounded 360° environments, supporting both compact indoor scenes and wide outdoor panoramas. Beyond their rendering capabilities, NeRFs inherently encode rich geometric and semantic cues, such as volumetric density and depth, that make them a promising substrate for scene understanding tasks, including segmentation, depth estimation, and semantic labelling. However, despite these advances, most NeRF-based systems remain specialised for view synthesis. Extending them toward semantic and interactive understanding, particularly In zero-shot 3D segmentation remains largely underexplored.

In contrast, 2D image segmentation has matured significantly with the advent of large-scale annotated datasets and general-purpose foundation models. The Segment Anything Model (SAM) [15], trained on billions of masks, demonstrates exceptional zero-shot generalisation: it can segment arbitrary objects from simple user prompts, such as points or bounding boxes without any task-specific fine-tuning. SAM’s success in 2D raises a compelling question: *Can we achieve comparable zero-shot segmentation performance in 3D scenes represented by NeRFs?*

Recent works such as SA3D [5] and ISRF [11] have attempted to extend SAM or feature-based approaches to 3D segmentation, respectively. ISRF [11] leverages DINO-derived features to inject semantic information into NeRF but relies on scene-specific optimisation, making it computationally expensive and slow. SA3D, while faster, still requires iterative optimisation using SAM masks and loses the inherent zero-shot generalisation that makes SAM attractive in the first place. These optimisation- and feature-matching-based methods highlight a trade-off between semantic expressiveness and efficiency, motivating the need for a training-free and interactive alternative.

We present **DivAS**, a Depth-interactive Voxel Aggregation Segmentation framework for NeRF that preserves SAMs’ zero-shot capability while enabling efficient 3D segmentation. DivAS refines SAM’s 2D masks using geometric priors derived from the NeRF depth field, without intro-

ducing any learnable parameters. Each SAM confidence map is adjusted through a depth-weighted prior that improves foreground-background separation, sharpens boundaries, and reduces errors in low-confidence areas. The refined masks are fused into a consistent 3D segmentation by a CUDA-optimized voxel aggregation kernel, which runs in under 200ms and supports feedback within a GUI.

To minimize annotation effort, DivAS uses Fibonacci sphere sampling to select a compact set of diverse anchor views across the 360° scene. Instead of labeling hundreds of dataset images, the user only annotates a few strategic views. Each view is further refined through a centroid-zoom mechanism that generates localized zoom-ins of fine or distinct object regions, mitigating SAM’s false negatives. The interactive GUI allows progressive refinement with continuous visual feedback, creating an intuitive user-in-the-loop segmentation experience.

The key contributions of this work are:

- **Optimization-Free Interactive 3D Segmentation:** We introduce DivAS, a training-free framework for interactive 3D segmentation that eliminates per-scene optimization while preserving SAM’s zero-shot generalization.
- **Depth-Weighted SAM Refinement:** We propose a depth-guided confidence refinement that leverages the NeRF’s learned depth field to improve mask precision and geometric consistency.
- **CUDA-Optimized Real-Time Voxel Fusion:** We design an efficient voxel fusion kernel that aggregates multi-view SAM masks into a consistent 3D grid within 150-200ms.
- **Efficient View Selection and Refinement Strategies:** We employ Fibonacci sphere sampling-based view selection and a centroid-zoom refinement strategy for balanced global coverage and high-fidelity local segmentation.

2. Related Work

2.1. Neural Radiance Field Representations

Neural Radiance Fields (NeRF) [20] represent 3D scenes implicitly and enable high-quality novel view synthesis through differentiable volume rendering. Subsequent variants have improved efficiency [6, 21], training speed [9, 10], and support for unbounded scenes [2]. We build upon Instant-NGP [21] for its real-time rendering capability, which is crucial for interactive segmentation.

2.2. 2D Segmentation Foundation Models

The field of 2D image segmentation, once dominated by CNN-based architectures [1, 7, 13], has matured significantly. The introduction of Vision Transformers [8] led to a new generation of models [4, 18, 25, 28] that achieve superior performance via global context modeling.

In 2D vision, segmentation has evolved from CNN-based models [1, 7, 13] to transformer-based architec-

tures [8, 18, 28] that leverage global context. The Segment Anything Model (SAM) [15] further established a foundation for zero-shot, prompt-based segmentation, inspiring numerous refinements [29, 30, 32]. Yet, transferring SAM’s 2D capabilities to 3D representations remains challenging. Our work bridges this gap by integrating SAM’s zero-shot priors with NeRF’s geometric structure for efficient, training-free 3D segmentation.

2.3. 3D Segmentation in NeRFs

Early works to segment NeRFs, such as SemanticNeRF [31], focused on training a separate semantic field alongside density and color. Other methods proposed interactive, user-in-the-loop segmentation [5, 11, 24] but typically require per-scene fine-tuning or optimisation. A parallel line of work focuses on feature alignment [16, 26], projecting 2D semantic features into the NeRF space, which can struggle with feature ambiguity and requires retraining.

More recently, methods have sought to lift 2D foundation models. LERF [14] and LangSplat [22] fuse CLIP [23] features with the 3D scene to enable language-driven queries. While powerful for semantic understanding, these methods target coarse, language-based concepts rather than the high-precision, interactive segmentation of arbitrary objects.

The most closely related works to DivAS are SA3D [5] and SANeRF-HQ [17], which also combine SAM with 3D representations. SA3D lifts 2D SAM masks to NeRF and employs a self-prompting mechanism to propagate segmentation across views. But errors in the initial mask or occluded regions can easily propagate. SANeRF-HQ [17] formulates the problem as a per-scene optimization, training a refinement network over SAM masks. This sacrifices SAM’s zero-shot generalization and incurs significant computation time. NTO3D [27] also leverages SAM but optimizes an implicit occupancy field from RGB-D inputs to reconstruct target objects in 3D. Unlike DivAS, it performs per-scene optimization for full object reconstruction rather than interactive segmentation, and does not use NeRF-based geometry. In contrast, DivAS is fully optimization-free. It preserves SAM’s zero-shot capability through a depth-weighted refinement guided step by NeRF geometry, replacing slow optimization with a real-time CUDA-accelerated voxel fusion kernel that aggregates geometrically consistent masks. This design achieves segmentation quality comparable to optimization-based methods while being 2-2.5x faster end-to-end, enabling a practical, interactive 3D workflow.

3. DivAS

We present **DivAS**, a training-free, interactive framework for performing 3D segmentation within Neural Radiance Fields (NeRFs). Our method employs a human-in-the-loop design that leverages the generalization capabilities of 2D

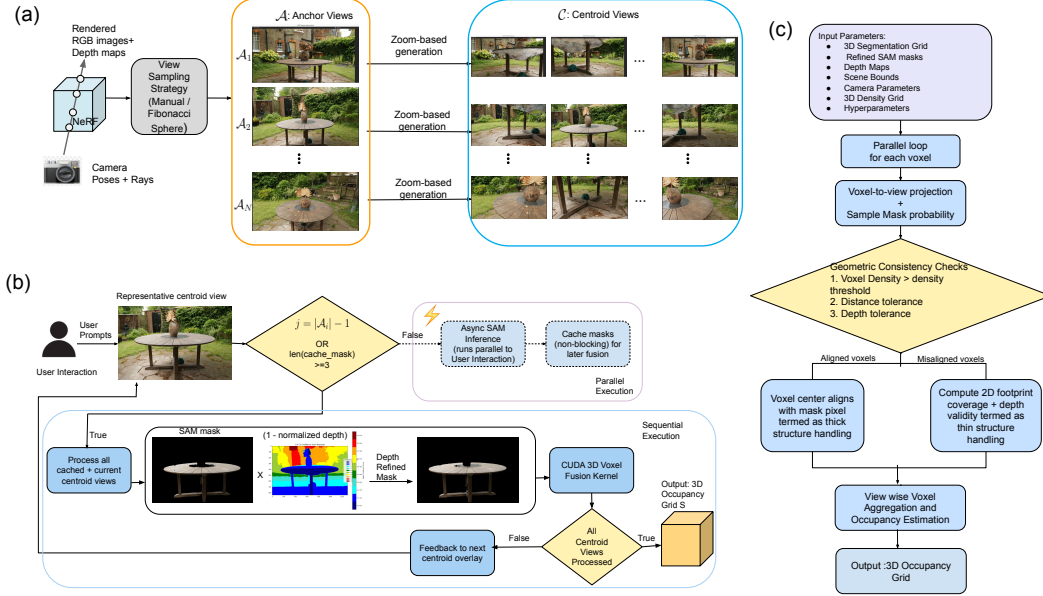


Figure 1. **Overview of DivAS.** (a) **Stage 1: Anchor and centroid view generation.** The user provides point prompts on global-scale *anchor views* to select distinct object regions. Each selected point generates a zoomed-in novel *centroid view* \mathcal{C} by moving the camera toward the point and setting it as the look-at target. (b) **Stage 2: Interactive centroid view processing and 3D fusion.** For each centroid view c_j in an anchor group \mathcal{A}_i , SAM inference runs asynchronously while the user continues interacting with subsequent views. When the cache holds at least three processed masks or the group ends, all cached and current masks are synchronized, refined using inverse-normalized NeRF depth maps, and fused by a CUDA-based 3D voxel kernel into a probabilistic occupancy grid \mathcal{S} . The resulting 3D mask is projected back onto the next centroid view for progressive refinement. (c) **CUDA voxel fusion kernel.** The kernel aggregates multi-view refined masks by enforcing geometric consistency through density, distance, and depth checks. It separately handles thick-structure voxels via direct projection alignment and thin-structure voxels through 2D footprint coverage, producing the final 3D occupancy grid.

foundation models in conjunction with NeRF’s geometric consistency. As shown in Sec. 2.3, the pipeline consists of two stages. In the first stage, the user selects a few anchor viewpoints and marks non-overlapping object regions to define localized centroid views. Each centroid view is rendered as a zoomed-in novel view from the NeRF, providing localized context around the selected points. Next, user prompts on these views trigger asynchronous SAM [15] inference for 2D mask generation. The resulting masks are refined using inverse depth maps from NeRF and fused in real-time by a CUDA-based voxel aggregation kernel to form a 3D occupancy grid. This fused 3D mask is projected back onto subsequent centroid views, enabling progressive feedback and iterative refinement across all viewpoints.

3.1. View Sampling Strategy

Our interactive framework supports both bounded and unbounded scenes. For bounded forward-facing scenes (e.g., LLFF [19]), most objects can be adequately covered using a few manually selected anchor viewpoints. In contrast, unbounded 360° scenes such as Mip-NeRF 360 demand greater viewpoint diversity to achieve full spatial coverage. To reduce user effort and ensure uniform angular distribution, we employ Fibonacci sphere sampling.

We adopt the Fibonacci lattice method [12], which distributes N points on a unit sphere with minimal angular clustering. This method produces low-discrepancy spherical coverage in $O(N)$ complexity and remains uniform even for small N (e.g., $N = 12$ for Mip-NeRF 360). From these, we select the top- K ($K = 5$) informative views for user annotation using a geometric ranking criterion.

Geometric View Ranking. The Fibonacci-sampled views are ranked according to an informativeness metric that balances three geometric factors: (i) **diversity**, measured as the mean pairwise angular separation to other views; (ii) **coverage**, encouraging proximity to canonical orientations (front, back, top, bottom, left, right); and (iii) **pitch extrema**, favoring top-down and bottom-up perspectives that improve 3D understanding. The final score for view i is a weighted sum: $I(i) = 0.4D_i + 0.3C_i + 0.3P_i$, where D_i , C_i , and P_i denote normalized diversity, coverage and pitch-extremity scores, respectively. The top-ranked views are retained as anchor viewpoints for subsequent interaction.

Handling Multi-Object scenes. While geometric ranking provides uniformly spaced anchor views, scenes in Mip-NeRF 360° are not always object-centric; target objects may be small, occluded, or far from the scene center. Because the ranking is purely geometry-driven and ignores se-

mantics, the top-5 views may not fully reveal the object. To handle such cases, our GUI allows switching to a larger pool of Fibonacci-sampled viewpoints. This allows users to manually select views that better expose the target object, thereby improving coverage in multi-object scenes.

3.2. View Generation

Users provide point prompts on sampled *anchor views* \mathcal{A} (see Sec. 2.3), obtained either manually or via the Fibonacci-sphere sampling strategy. Each anchor view offers a global perspective of the scene. In LLFF scenes, where geometry is mostly forward-facing, a few anchor views with multiple point prompts are sufficient.

For 360° unbounded scenes, selecting two to three distant, non-overlapping points per anchor typically achieves complete object coverage. Following SAM [15], whose mask decoder outputs a low-resolution (256×256) mask. To improve segmentation precision, we introduce *centroid views* localized, zoomed-in renderings centered around the user selected points. These zoomed views enlarge the object on the image plane, improving segmentation precision and reducing SAM false negatives on thin or distant structures. Each centroid view is generated by moving the camera toward the selected point along its viewing direction while setting it as the look-at target. Typical zoom factors are 0.67 for LLFF and 0.47 for Mip-NeRF, though they are interactively adjustable. Formally,

$$\mathcal{C} = \bigcup_{i=1}^A \bigcup_{j=1}^K \mathcal{A}_{ij}, \quad (1)$$

where A and K denote the number of anchor views and centroid points per anchor, respectively. Additional procedural details are provided in the supplementary material. The centroid-view pose is obtained by back-projecting the 2D prompt (w, h) into world coordinates using the camera intrinsics \mathbf{K} and extrinsics \mathbf{P} , as in Eq. (6) of [17]. Unlike [17], which relies on expected depth from the volumetric rendering integral, we use the depth of the maximum-weight sample along the ray. This produces a sharper surface estimate and is computed in $\mathcal{O}(1)$ within NeRF’s ray-marching loop.

3.3. Parallel Execution

A key challenge in interactive 3D segmentation within NeRFs is SAM’s high per-image inference time, which limits responsiveness. To address this, we implement an asynchronous strategy that overlaps SAM inference with user interaction. While the user provides point prompts on the current centroid view c_i , SAM concurrently processes preceding views $\{c_{i-1}, c_{i-2}\}$ in the background. The resulting masks are cached until specific synchronization conditions are met. The system switches from asynchronous to sequential execution when either (i) the current centroid view c_i

is the last in its anchor group \mathcal{A}_i , or (ii) the cache holds at least three processed SAM masks. At that point, all pending inferences, including c_i , are completed before the next fusion step. Otherwise, SAM continues processing in parallel with ongoing user input. This overlapping design provides progressive 3D feedback to the user without requiring full per-view inference completion.

3.4. Depth Refined Mask

Centroid views improve SAM’s precision by enlarging object scale, yet SAM often produces false positives and boundary artifacts at this scale. Similar observations were made in SANeRF-HQ [17], which reported that segmentation errors in both 2D and 3D are more likely to occur near object boundaries. Motivated by this, we refine SAM masks using NeRF’s depth map as a geometric prior. Each SAM confidence map \mathbf{M}_{ij} is weighted by the inverse normalized depth $\hat{\mathbf{Z}}_{ij} = \frac{Z_{ij} - \min(\mathbf{Z}_{ij})}{\max(\mathbf{Z}_{ij}) - \min(\mathbf{Z}_{ij})}$ to enhance boundary localization and spatial consistency.

$$\tilde{\mathbf{M}}_{ij} = \mathbf{M}_{ij} \odot (1 - \hat{\mathbf{Z}}_{ij}), \quad (2)$$

Here, $\tilde{\mathbf{M}}_{ij}$ is the depth-weighted mask for centroid view j of anchor group \mathcal{A}_i . This depth-guided weighting embeds scene geometry priors without additional learning, yielding sharper and more consistent masks near object boundaries. Qualitative results are provided in the supplementary.

3.5. 3D Voxel Fusion Kernel

3.5.1. Inputs to the 3D Voxel Fusion Kernel

The CUDA kernel fuses multi-view, depth-refined SAM masks into a unified 3D occupancy grid \mathbf{S} , where each voxel stores a segmentation probability $p \in (0, 1)$. It takes as input depth-refined masks \mathbf{M} , a density grid ρ , and camera parameters $\{\mathbf{K}, \mathbf{T}\}$ within scene bounds b . For each view, the following quantities are also computed during NeRF ray-sampling:

Cumulative-weight cutoff (τ_{cw}): Threshold on accumulated transmittance along each NeRF ray, marking where foreground density saturates and background sampling is stopped. \mathbf{D}_{\min} : Depth at which the accumulated ray weight first exceeds $1e^{-4}$. \mathbf{D}_{\max} : Depth of the first sample where cumulative weight $\geq \tau_{\text{cw}}$. \mathbf{D}_{exp} : Expected depth under the truncated accumulation up to τ_{cw} . N_{samples} : Number of NeRF samples contributing until the cumulative weight reaches τ_{cw} .

Parameter	Purpose
<code>base_tolerance_multiplier</code> γ	Base scale for depth tolerance used in geometric checks.
<code>per_sample_bonus</code> β	Incremental relaxation added per supporting depth sample.
<code>max_bonus</code> b_{\max}	Upper bound on the accumulated tolerance bonus.
<code>depth_range_factor</code> λ_{range}	Used to control the distance tolerance check.
<code>density_thresh</code> ρ_{thresh}	Density required for a voxel to be considered valid.
<code>thin_density_thresh</code> $\rho_{\text{thin},\text{thresh}}$	Higher density threshold used to detect thin structures.
<code>thin_percent_cover</code> $\rho_{\text{percent},\text{cover},\text{thresh}}$	Fractional coverage of voxel by the masked pixels.

Table 1. Kernel hyperparameters used which is fixed per dataset.

3.5.2. Voxel to view Projection

Each voxel x in the 3D grid \mathbf{S} is processed in parallel, with one CUDA thread per voxel. Its center position x_c is projected onto each centroid view using i using the camera intrinsics \mathbf{K}_i and extrinsics \mathbf{T}_i : $(u_x^i, v_x^i) = \pi_i(\mathbf{x}_c)$, where $\pi_i(\cdot)$ denotes the projection from world to normalized image coordinates. Voxels with $u_x^i \notin [0, 1] \vee v_x^i \notin [0, 1]$ are skipped. Otherwise, coordinates are mapped to discrete pixel indices using (w, h) image resolution as $x_p = \lfloor w \ u_x^i \rfloor, \ y_p = \lfloor h \ v_x^i \rfloor$, and corresponding SAM mask probability for voxel x and view i is then sampled as:

$$m_x^i \leftarrow \mathbf{M}^i(x_p, y_p)$$

Voxels with $m_x^i \geq 0.5$ proceed to geometric validation, while those below this threshold are routed to the thin-structure path.

3.5.3. Geometric Consistency Checks

If a voxel x passes the mask threshold. We ensure that its NeRF density is valid: $\rho_x \geq \rho_{\text{thresh}}$ where ρ_x denotes the voxel density.

Ray-voxel alignment We enforce geometric consistency by measuring the distance between the voxel center and the image ray corresponding to pixel (u_x^i, v_x^i) . The ray origin and direction are derived as: $\mathbf{o}_i, \mathbf{d}_i = \pi_{\text{uv_to_ray}}(u_x^i, v_x^i, \mathbf{K}_i, \mathbf{T}_i), \ \hat{\mathbf{d}}_i = \frac{\mathbf{d}_i}{\|\mathbf{d}_i\|}$ where, $\mathbf{o}_i, \mathbf{d}_i$ represent the ray origin and normalized direction.

The voxel-to-ray depth is computed as the projection: $t_{\text{proj}} = \langle \mathbf{x}_c - \mathbf{o}_i, \hat{\mathbf{d}}_i \rangle$ and is clamped to the valid NeRF surface interval:

$$t_c = \text{clamp}(t_{\text{proj}}, \mathbf{D}_{\min}(x_p, y_p), \mathbf{D}_{\max}(x_p, y_p)),$$

which ensures that the voxel lies within the ray segment corresponding to the rendered surface. The closest point on the segment of the ray is then: $\mathbf{p}_c = \mathbf{o}_i + \hat{\mathbf{d}}_i t_c$ mapped through contraction for unbounded scenes. The geometric deviation used for consistency testing is:

$$\delta_x^i = \|\mathbf{x}_c - \mathbf{p}_c\|. \quad (3)$$

This is the value on which the distance tolerance criterion is applied for geometric consistency.

Depth-gradient factor. We adapt the distance tolerance using a depth-gradient term $g_p^i = \pi_{\text{depth_gradient}}(x_p, y_p, \mathbf{D}_{\min}, \mathbf{D}_{\max})$, which yields a value in $[0, 1]$ —large on flat regions and small near boundaries. Its full expression is included in the supplementary.

Distance tolerance: We define a spatial proximity threshold between a voxel and its corresponding ray as:

$$\begin{aligned} \tau_{\text{spatial}} &= \Delta_x \cdot g_p^i(x_p, y_p) \\ &+ \lambda_{\text{range}}(\mathbf{D}_{\max}(x_p, y_p) - \mathbf{D}_{\min}(x_p, y_p)) \end{aligned} \quad (4)$$

where $\Delta_x = \frac{2B_\ell}{G}$ is the voxel size at cascade level ℓ following the multi-resolution grid in [21]. λ_{range} is a scene-dependent hyperparameter (listed in Tab. 1). This adap-

tively increases the tolerance in smooth regions and decreases it at depth edges.

Depth tolerance: To prevent background leakage, we impose a depth consistency check on each voxel. The voxel depth x_d is computed along the camera’s forward axis as: $x_d = \pi_{\text{voxel_depth}}(\mathbf{x}_c, \mathbf{K}_i, \mathbf{T}_i)$ $\pi_{\text{voxel_depth}}(\cdot)$ projects the voxel into the camera coordinate frame. The depth tolerance adapts to the NeRF sampling density $\mathbf{N}_{\text{samples}}(x_p, y_p)$: $b = \min(\beta \cdot \mathbf{N}_{\text{samples}}(x_p, y_p), b_{\max})$, $\tau_{\text{depth}} = (\gamma + b)\Delta_x$, with β, b_{\max}, γ defined in Tab. 1. A voxel x is considered geometrically consistent if

$$\delta_x^i \leq \tau_{\text{spatial}} \wedge |x_d - \mathbf{D}_{\text{exp}}| \leq \tau_{\text{depth}} \quad (5)$$

Voxels satisfying both conditions follow the *thick-structure* path for depth-weighted score aggregation, while others are handled by the thin-structure refinement step.

3.5.4. Depth-weighted Vote Aggregation

After a voxel passes the geometric consistency checks, its contribution to the 3D occupancy grid is weighted according to depth. This design follows the volumetric rendering principle in NeRF: along each camera ray, most of the density accumulates near the surface intersection, while contributions from distant samples fade. Hence, voxels projected to the expected surface center should have higher influence than those at the depth boundaries.

Depth-weight formulation. We compute the midpoint and half-width of this segment as: $\mu_d = \frac{\mathbf{D}_{\min}(x_p, y_p) + \mathbf{D}_{\max}(x_p, y_p)}{2}, \ h_d = \max(\frac{\mathbf{D}_{\max} - \mathbf{D}_{\min}}{2}, \epsilon)$, where ϵ prevents division by zero for thin ranges. For a voxel projected at clamped ray depth t_c , the normalized offset from the range center is: $r = \frac{|t_c - \mu_d|}{h_d}$. We assign a depth-based confidence weight

$$w_{\text{depth}} = \exp(-\alpha_1 \cdot r^2), \quad (6)$$

where α_1 is a fixed falloff constant controlling how quickly confidence decays with depth distance. Voxels near the range midpoint ($r \approx 0$) thus receive higher weights, while those farther away are smoothly down-weighted, approximating a Gaussian attenuation around the true surface.

Vote accumulation: For each valid voxel-view pair (x, i) with refined SAM mask probability m_x^i , the kernel accumulates weighted votes: $\text{weighted_votes}_x += m_x^i \cdot w_{\text{depth}}$, $\text{total_weight}_x += w_{\text{depth}}$. After processing all views, the final voxel occupancy probability is obtained by normalization:

$$p_x = \frac{\text{weighted_votes}_x}{\text{total_weight}_x} \quad (7)$$

Because the weights are normalized, the exact choice of α_1 only affects the relative sharpness of the weighting and not the overall scale, yielding stable and consistent fusion across all scenes.

3.5.5. Thin-structure handling

Thin or semi-transparent regions (e.g., ribs, wires, edges) are frequently missed by the main geometric consistency check because they project to only a few pixels, leaving no voxel centers aligned with confident SAM predictions. To improve recall of such fine structures, we introduce a dedicated thin-structure path applied only to voxels likely to belong to slender, high-density regions.

A voxel is marked as a thin-structure candidate if it satisfies three criteria: (i) it appears in close or zoomed-in views (smaller effective scale), (ii) its corresponding SAM mask probability is non-trivial (> 0.1), and (iii) its NeRF-predicted density exceeds $\rho_{\text{thin_thresh}}$. These constraints suppress background activations while targeting geometrically plausible thin components. For each candidate voxel, the thin-structure check evaluates its local 2D footprint within the image through consistent support from neighboring pixels.

Voxel footprint projection Given a voxel x with size Δ_x in centroid view i , we represent its eight corners as:

$$\mathbf{x}_j^i = \mathbf{x}_c^i + \frac{\Delta_x}{2} \boldsymbol{\epsilon}_j, \quad \boldsymbol{\epsilon}_j \in \{-1, +1\}^3, \quad j = 1, \dots, 8.$$

Each corner is projected into the image plane: $(u_j^x, v_j^x) = \pi_i(\mathbf{x}_j^i)$. The voxel's projected footprint defines a bounding box: $u_{\min} = \min_j u_j^x, u_{\max} = \max_j u_j^x, v_{\min} = \min_j v_j^x, v_{\max} = \max_j v_j^x$. Converted to discrete pixel indices: $x_{\text{start}} = \lfloor w u_{\min} \rfloor, x_{\text{end}} = \lfloor w u_{\max} \rfloor, y_{\text{start}} = \lfloor h v_{\min} \rfloor, y_{\text{end}} = \lfloor h v_{\max} \rfloor$.

Per-pixel consistency Let the voxel's depth along the ray be $x_d = \pi_{\text{voxel_depth}}(\mathbf{x}_c, \mathbf{K}_i, \mathbf{T}_i)$. For each pixel (x_p, y_p) within the footprint, we compute an adaptive depth tolerance:

$$b(x_p, y_p) = \min(b_{\max}, \beta N_{\text{samples}}(x_p, y_p)),$$

$$\tau_{\text{depth}}(x_p, y_p) = (2\gamma + b(x_p, y_p)) \Delta_x$$

where β, b_{\max}, γ defined in Tab. 1. A pixel is considered *supportive* if:

$$\mathbf{M}^i(x_p, y_p) > 0.5 \wedge |x_d - \mathbf{D}_{\text{exp}}(x_p, y_p)| \leq \tau_D(x_p, y_p).$$

Coverage and confidence Let support_count be the number of supportive pixels and n_{pixels} the total pixels within the footprint. The fraction of consistent coverage is:

$$p_{\text{covered}} = \frac{\text{support_count}}{n_{\text{pixels}}}, \quad m_{\max} = \max_{x, y \in \text{footprint}} \mathbf{M}^i(x, y)$$

The thin-structure confidence for voxel x in view i is:

$$t_x^i = \begin{cases} m_{\max}, & \text{if } p_{\text{covered}} \geq \rho_{\text{percent_cover_thresh}}, \\ p_{\text{covered}}, & \text{otherwise.} \end{cases}$$

This confidence $t_x^i \in [0, 1]$ provides partial credit for delicate structures, improving recall without compromising geometric precision.

3.6. Compact fusion

Combining the thick and thin structure views, the fused probability for each voxel is computed as follows. Let:

- \mathcal{C}_v : centroid-views from thick-structure path.
- \mathcal{T}_v : views contributing thin-structure evidence.

- $m_v^{(c)}$: refined SAM confidence from view $c \in \mathcal{C}_v$.
- $t_v^{(t)}$: thin-structure score from view $t \in \mathcal{T}_v$.
- $w_v^{(c)}$: depth alignment weight for view c .
- ρ_{thin} thin-structure acceptance threshold (0.6).
- ε a small constant for numerical stability.

The fused probability for voxel v is:

$$S(v) = \begin{cases} \frac{\sum_{c \in \mathcal{C}_v} m_v^{(c)} w_v^{(c)} + \sum_{t \in \mathcal{T}_v} \mathbf{1}[t_v^{(t)} \geq \rho_{\text{thin}}] t_v^{(t)}}{\sum_{c \in \mathcal{C}_v} w_v^{(c)} + \sum_{t \in \mathcal{T}_v} \mathbf{1}[t_v^{(t)} \geq \rho_{\text{thin}}]}, & \text{if denominator} > \varepsilon, \\ 0, & \text{otherwise.} \end{cases}$$

A thin-structure view contributes to the voxel's probability only if its mask confidence exceeds the threshold $\rho_{\text{thin}} = 0.6$, meaning that even a single strong mask activation at this level is treated as evidence of object presence in that voxel.

4. Experiments

We now describe our experimental setup and present both quantitative and qualitative results. Our approach is compared with existing state-of-the-art methods.

4.1. Datasets

We evaluate our method on two types of scenes: bounded and unbounded. For bounded scenes, we use the LLFF [19] dataset, which contains multiple forward-facing real-world scenes. For unbounded scenes, we use the Mip-NeRF 360° [3] dataset, which includes complex, large-scale environments. To enable quantitative evaluation, we use the NVOS [24] dataset. NVOS provides hand-curated ground-truth mask for a single test view per scene in LLFF. For Mip-NeRF 360°, no true mask exist, so we adopt the pseudo-ground truth masks released by [17].

4.2. Ablation Studies

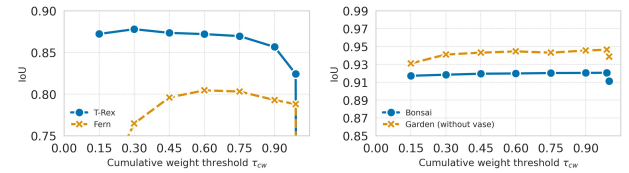


Figure 2. IoU vs cumulative-weight(τ_{cw}) target

Cumulative weight(τ_{cw}): We evaluate τ_{cw} on scenes with narrow (*Trex*) and wide (*Fern*) depth ranges from LLFF, and on *Bonsai* and *Garden* from Mip-NeRF 360°. As shown in Fig. 2, IoU remains stable for $\tau_{\text{cw}} \in [0.3, 0.75]$, while large values (≥ 0.9) sharply degrade performance by widening the valid depth interval and activating background voxels. Although $\tau_{\text{cw}} = 0.6$ slightly improves *Trex*, *Fern* shows cleaner masks at 0.75. LLFF (uniform sampling), is more sensitive to τ_{cw} , whereas in Mip-NeRF 360° (hierarchical sampling) remains nearly constant. We therefore use $\tau_{\text{cw}} = 0.75$ as a stable choice across datasets.

Due to space constraints, we provide extended ablations, qualitative comparisons, and additional analysis in the supplementary material.

Scene	Thin: w	Thin: w/o	Depth: w	Depth: w/o
Trex	0.869	0.673	0.869	0.867
Fern	0.803	0.814	0.803	0.801
Horns_left	0.935	0.883	0.935	0.929
Bonsai	0.920	0.915	0.920	0.918
Garden (w/o vase)	0.943	0.899	0.943	0.946

Table 2. Combined ablation showing the effect of (i) thin-structure handling and (ii) depth-based SAM weighting via IoU scores.

Scene	Fibonacci (mIoU)	Manual (mIoU)
Bonsai	0.9203	0.9205
Garden (without vase)	0.9431	0.9501
Garden (with vase)	0.9364	0.9319
Kitchen (Lego)	0.9170	0.9273
Counter (flowerpot)	0.8902	0.8965
Room (chair)	0.8703	0.8953
Mean	0.913	0.920

Table 3. View selection ablation in Mip-NeRF 360°.

Fibonacci vs Manual view selection: Our pipeline supports both automated Fibonacci sampling and manual view selection. By default, we employ Fibonacci sampling as it provides uniform multi-view coverage and saves user effort. As shown in Table 3, this automated approach achieves a performance mean (0.913 mIoU) that is comparable to manual selection mean (0.920 mIoU), demonstrating its effectiveness without a significant performance trade-off. Manual selection offers slight gains in non-object-centric or highly occluded scenes by allowing users to choose views that better expose the target. Hence, we use Fibonacci sampling for our main evaluation to ensure reproducibility, while offering manual selection as an effective option for challenging scenarios.

Thin-structure handling. Table 2 highlights the importance of our thin-structure path. Scenes with fine geometry, such as *Trex* and *Garden*, show large IoU drops when the module is removed (e.g., 0.869 → 0.673 in *Trex*), confirming the need for the 2D footprint check to recover thin details missed by the stricter consistency test.

In *Fern*, the module slightly reduces IoU (0.803 → 0.814), which we attribute to NeRF’s higher depth uncertainty in this scene rather than an issue with the method itself. Overall, the small trade-off in such cases is outweighed by the substantial gains on thin and delicate structures.

No depth weighting: As shown in Tab. 2, removing the NeRF depth-based weighting results in a negligible quantitative change but a clear qualitative degradation. Without depth weighting, zoomed regions exhibit faint ghost artifacts—background voxels falsely activated as foreground. This occurs because denser sampling in zoomed views increases false SAM responses on nearby background pixels. Depth-based weighting suppresses these spurious ac-

tivations by downscaling the mask confidence for depth-inconsistent pixels, resulting in cleaner, more localized segmentation.

4.3. Quantitative Results

NVOS Dataset: This dataset provide a single reference image with user strokes and a ground-truth mask for another view. We compare our method, DivAS, against state-of-the-art optimization-based baselines [5, 17]. To ensure fairness, we run each method following its official pipeline. The resulting segmentation is then compared against the NVOS ground-truth mask for that held-out validation view.

Scene	SA3D		SANeRF-HQ		Ours	
	IoU ↑	Acc ↑	IoU ↑	Acc ↑	IoU ↑	Acc ↑
Fern	0.822	0.943	0.825	0.944	0.803	0.933
Fortress	0.969	0.994	0.972	0.995	0.975	0.995
Horns_center	0.973	0.995	0.969	0.995	0.978	0.996
Horns_left	0.936	0.996	0.939	0.996	0.935	0.996
Orchids	0.880	0.979	0.778	0.956	0.895	0.982
Trex	0.831	0.977	0.841	0.979	0.869	0.982
Mean	0.902	0.981	0.887	0.978	0.909	0.981

Table 4. Quantitative comparison on the NVOS dataset. We report IoU and pixel Accuracy (Acc) for each method.

LLFF dataset. As shown in Tab. 4, our method achieves the highest mean IoU(Intersection-over-union)(0.909) and comparable pixel accuracy (0.981) among all baselines. The consistent improvement over SA3D [5] highlights the advantage of interactive centroid-view refinement in reducing false negatives on fine object details. Notably, SANeRF-HQ [17] shows a sharp performance drop in the *Orchids* scene. It incorrectly segments unprompted flower buds that appear visually similar to the user-selected petals. This over-segmentation arises from its global optimization process, which lacks fine spatial prompt control. In contrast, our centroid-view design restricts segmentation to the prompted regions, enabling localized refinement. As a result, our method avoids false activations on nearby, visually similar structures. These results confirm that spatially guided prompts and voxel-level fusion yield stable and accurate segmentation across forward-facing scenes.

Mip-360° Dataset: We follow the evaluation protocol from [17] reserving held-out test views containing the target object. Mean IoU (mIoU) and mean pixel accuracy (mAcc) are reported across these test views to assess multi-view consistency. As shown in Tab. 5, SA3D performs well in simple, object-centric settings (*Kitchen*), but struggles in occluded scenes (*Garden*) with vase, *Counter* with a flowerpot, where single-view prompts fail to capture the target region across multiple viewpoints. Our approach maintains geometric consistency under such occlusions by fusing multi-view cues through a 3D voxel kernel, leading to smoother and more coherent reconstructions. Although

Scene	SA3D		SANeRF-HQ		Ours(Fibonacci)	
	mIoU ↑	mAcc ↑	mIoU ↑	mAcc ↑	mIoU ↑	mAcc ↑
Bonsai	0.912	0.991	0.906	0.989	0.920	0.991
Garden(without_vase)	0.903	0.982	0.952	0.991	0.943	0.990
Garden(with_vase)	0.758	0.954	0.928	0.988	0.936	0.988
Kitchen	0.97	0.996	0.836	0.978	0.917	0.988
Counter(flowerpot)	0.364	0.952	0.902	0.994	0.890	0.993
Room(chair)	0.831	0.977	0.952	0.999	0.87	0.996
Mean	0.790	0.975	0.913	0.990	0.913	0.991

Table 5. Quantitative comparison on the Mip-360° dataset. We report mean Intersection-over-Union (mIoU) and mean pixel Accuracy (mAcc) for each method.

pseudo ground truth masks from SANeRF-HQ occasionally penalize our IoU in scenes like *Counter*, qualitative results (see Fig. 4) show that our predictions align better with the actual object geometry, particularly in thin or partially occluded structures. Overall, our method matches SANeRF-HQ [17] in quantitative accuracy, comparable to SANeRF-HQ, while being an order of magnitude faster. This demonstrates the effectiveness of amortized (i.e., optimization-free) 3D fusion without per-scene optimization.

4.4. Qualitative Analysis

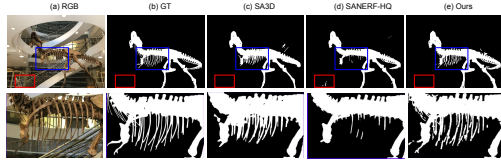


Figure 3. Results of different methods on LLFF

As shown in Fig. 3, we visualize segmentation results for the *Trex* object across different methods. SA3D captures fine structures like ribs but misses global parts such as the tail, and slightly leaks into the background (row 2). SANeRF-HQ recovers the complete shape but fails on thin features like the ribs and hands. It also exhibits over-segmentation by incorrectly marking background regions with similar appearance, highlighted in the red box (row 1). This behavior aligns with its false-positive tendency observed in the *Orchids* scene. Our method preserves both global structure and delicate parts, such as ribs and hands, while avoiding false activations and over-segmentation.

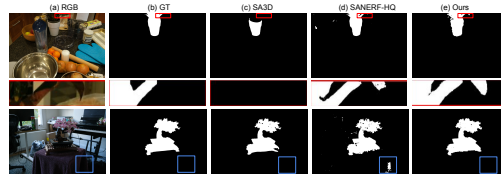


Figure 4. Results of different methods on MIP-360°

In Fig. 4, we compare methods on the *Counter (flowerpot)* and *Bonsai* scenes from Mip-NeRF 360°. In the first row, the red box marks a region where the pseudo ground

truth misses part of the flowerpot’s leaf. The zoomed-in crops (row 2) show that our method better preserves object boundaries and maintains multi-view geometric consistency. SA3D misses occluded plant regions due to its single-view prompting strategy. In the third row *Bonsai*, SANeRF-HQ again shows over-segmentation, assigning distant background areas as part of the target object (blue box). Our method produces sharper, more localized masks that are consistent with the true object geometry.

4.5. Compute and Runtime Analysis:

Runtime Analysis. All experiments are conducted on a single NVIDIA A100 GPU. Interactive latency is dominated by NeRF rendering (~ 1.3 s per view). SAM inference (~ 0.45 s) is run asynchronously and overlaps with user interaction (15–20 s per click). The CUDA fusion kernel adds only 150–200 ms per update. End-to-end, DivAS completes a typical scene in 4–6 minutes, while SANeRF-HQ takes ~ 10 minutes, giving a 2–2.5 \times speed-up. If prompts and views are pre-cached, the compute time drops to ~ 10 s per scene, highlighting the efficiency of our optimization-free design. Unlike optimization-based baselines, whose cost grows with the number of training views, DivAS remains largely independent of dataset size. Additional timing details are provided in the supplementary.

5. Limitations

DivAS inherits limitations from the underlying NeRF and SAM models. Since our pipeline relies on a pre-trained NeRF, the segmentation quality degrades in scenes with poor geometry, especially in non-object-centric layouts, where the target receives few samples, leading to depth ambiguity and occasional background leakage. Our method also relies on SAM for initial masks: while centroid zoom helps suppress false positives and mitigate false negatives, recovering from all failure cases remains challenging. Future work could explore adaptive NeRF sampling to address these challenges.

6. Conclusion

We presented DivAS, a training-free, zero-shot framework for interactive 3D segmentation built atop pre-trained NeRF reconstructions. DivAS requires no optimization or fine-tuning beyond the standard NeRF training used for scene reconstruction, yet achieves performance comparable to optimization-based approaches across diverse datasets. By combining NeRF-derived geometric priors with zero-shot 2D segmentation, DivAS enables fast and accurate 3D object extraction. We expect this direction to support future tools for interactive, optimization-free 3D editing and scene understanding.

References

[1] Vijay Badrinarayanan, Alex Kendall, and Roberto Cipolla. Segnet: A deep convolutional encoder-decoder architecture for image segmentation. *IEEE transactions on pattern analysis and machine intelligence*, 39(12):2481–2495, 2017. 2

[2] Jonathan T Barron, Ben Mildenhall, Matthew Tancik, Peter Hedman, Ricardo Martin-Brualla, and Pratul P Srinivasan. Mip-nerf: A multiscale representation for anti-aliasing neural radiance fields. In *Proceedings of the IEEE/CVF international conference on computer vision*, pages 5855–5864, 2021. 2

[3] Jonathan T Barron, Ben Mildenhall, Dor Verbin, Pratul P Srinivasan, and Peter Hedman. Mip-nerf 360: Unbounded anti-aliased neural radiance fields. In *Proceedings of the IEEE/CVF conference on computer vision and pattern recognition*, pages 5470–5479, 2022. 1, 6

[4] Mathilde Caron, Hugo Touvron, Ishan Misra, Hervé Jégou, Julien Mairal, Piotr Bojanowski, and Armand Joulin. Emerging properties in self-supervised vision transformers. In *Proceedings of the IEEE/CVF international conference on computer vision*, pages 9650–9660, 2021. 2

[5] Jiazhong Cen, Zanwei Zhou, Jiemin Fang, Wei Shen, Lingxi Xie, Dongsheng Jiang, Xiaopeng Zhang, Qi Tian, et al. Segment anything in 3d with nerfs. *Advances in Neural Information Processing Systems*, 36:25971–25990, 2023. 1, 2, 7

[6] Anpei Chen, Zexiang Xu, Andreas Geiger, Jingyi Yu, and Hao Su. Tensorf: Tensorial radiance fields. In *European conference on computer vision*, pages 333–350. Springer, 2022. 2

[7] Liang-Chieh Chen, George Papandreou, Iasonas Kokkinos, Kevin Murphy, and Alan L Yuille. Deeplab: Semantic image segmentation with deep convolutional nets, atrous convolution, and fully connected crfs. *IEEE transactions on pattern analysis and machine intelligence*, 40(4):834–848, 2017. 2

[8] Alexey Dosovitskiy. An image is worth 16x16 words: Transformers for image recognition at scale. *arXiv preprint arXiv:2010.11929*, 2020. 2

[9] Sara Fridovich-Keil, Alex Yu, Matthew Tancik, Qinhong Chen, Benjamin Recht, and Angjoo Kanazawa. Plenoxels: Radiance fields without neural networks. In *Proceedings of the IEEE/CVF conference on computer vision and pattern recognition*, pages 5501–5510, 2022. 2

[10] Stephan J Garbin, Marek Kowalski, Matthew Johnson, Jamie Shotton, and Julien Valentin. Fastnerf: High-fidelity neural rendering at 200fps. In *Proceedings of the IEEE/CVF international conference on computer vision*, pages 14346–14355, 2021. 2

[11] Rahul Goel, Dhawal Sirikonda, Saurabh Saini, and PJ Narayanan. Interactive segmentation of radiance fields. In *Proceedings of the IEEE/CVF conference on computer vision and pattern recognition*, pages 4201–4211, 2023. 1, 2

[12] Álvaro González. Measurement of areas on a sphere using fibonacci and latitude–longitude lattices. *Mathematical geosciences*, 42(1):49–64, 2010. 3

[13] Kaiming He, Georgia Gkioxari, Piotr Dollár, and Ross Girshick. Mask r-cnn. In *Proceedings of the IEEE international conference on computer vision*, pages 2961–2969, 2017. 2

[14] Justin Kerr, Chung Min Kim, Ken Goldberg, Angjoo Kanazawa, and Matthew Tancik. Lerp: Language embedded radiance fields. In *Proceedings of the IEEE/CVF international conference on computer vision*, pages 19729–19739, 2023. 2

[15] Alexander Kirillov, Eric Mintun, Nikhila Ravi, Hanzi Mao, Chloe Rolland, Laura Gustafson, Tete Xiao, Spencer Whitehead, Alexander C Berg, Wan-Yen Lo, et al. Segment anything. In *Proceedings of the IEEE/CVF international conference on computer vision*, pages 4015–4026, 2023. 1, 2, 3, 4

[16] Sosuke Kobayashi, Eiichi Matsumoto, and Vincent Sitzmann. Decomposing nerf for editing via feature field distillation. *Advances in neural information processing systems*, 35:23311–23330, 2022. 2

[17] Yichen Liu, Benran Hu, Chi-Keung Tang, and Yu-Wing Tai. Sanerf-hq: Segment anything for nerf in high quality. In *Proceedings of the IEEE/CVF Conference on Computer Vision and Pattern Recognition*, pages 3216–3226, 2024. 2, 4, 6, 7, 8

[18] Ze Liu, Yutong Lin, Yue Cao, Han Hu, Yixuan Wei, Zheng Zhang, Stephen Lin, and Baining Guo. Swin transformer: Hierarchical vision transformer using shifted windows. In *Proceedings of the IEEE/CVF international conference on computer vision*, pages 10012–10022, 2021. 2

[19] Ben Mildenhall, Pratul P Srinivasan, Rodrigo Ortiz-Cayon, Nima Khademi Kalantari, Ravi Ramamoorthi, Ren Ng, and Abhishek Kar. Local light field fusion: Practical view synthesis with prescriptive sampling guidelines. *ACM Transactions on Graphics (ToG)*, 38(4):1–14, 2019. 3, 6

[20] Ben Mildenhall, Pratul P Srinivasan, Matthew Tancik, Jonathan T Barron, Ravi Ramamoorthi, and Ren Ng. Nerf: Representing scenes as neural radiance fields for view synthesis. In *European Conference on Computer Vision*, pages 405–421. Springer, 2020. 1, 2

[21] Thomas Müller, Alex Evans, Christoph Schied, and Alexander Keller. Instant neural graphics primitives with a multiresolution hash encoding. 2022. 2, 5

[22] Minghan Qin, Wanhua Li, Jiawei Zhou, Haoqian Wang, and Hanspeter Pfister. Langsplat: 3d language gaussian splatting. In *Proceedings of the IEEE/CVF Conference on Computer Vision and Pattern Recognition*, pages 20051–20060, 2024. 2

[23] Alec Radford, Jong Wook Kim, Chris Hallacy, Aditya Ramesh, Gabriel Goh, Sandhini Agarwal, Girish Sastry, Amanda Askell, Pamela Mishkin, Jack Clark, et al. Learning transferable visual models from natural language supervision. In *International conference on machine learning*, pages 8748–8763. PMLR, 2021. 2

[24] Zhongzheng Ren, Aseem Agarwala, Bryan Russell, Alexander G Schwing, and Oliver Wang. Neural volumetric object selection. In *Proceedings of the IEEE/CVF conference on computer vision and pattern recognition*, pages 6133–6142, 2022. 2, 6

[25] Robin Strudel, Ricardo Garcia, Ivan Laptev, and Cordelia Schmid. Segmenter: Transformer for semantic segmentation. In *Proceedings of the IEEE/CVF international conference on computer vision*, pages 7262–7272, 2021. 2

- [26] Vadim Tschernezki, Iro Laina, Diane Larlus, and Andrea Vedaldi. Neural feature fusion fields: 3d distillation of self-supervised 2d image representations. In *2022 International Conference on 3D Vision (3DV)*, pages 443–453. IEEE, 2022. [2](#)
- [27] Xiaobao Wei, Renrui Zhang, Jiarui Wu, Jiaming Liu, Ming Lu, Yandong Guo, and Shanghang Zhang. Nto3d: Neural target object 3d reconstruction with segment anything. In *Proceedings of the IEEE/CVF Conference on Computer Vision and Pattern Recognition*, pages 20352–20362, 2024. [2](#)
- [28] Enze Xie, Wenhui Wang, Zhiding Yu, Anima Anandkumar, Jose M Alvarez, and Ping Luo. Segformer: Simple and efficient design for semantic segmentation with transformers. *Advances in neural information processing systems*, 34: 12077–12090, 2021. [2](#)
- [29] Yunyang Xiong, Bala Varadarajan, Lemeng Wu, Xiaoyu Xiang, Fanyi Xiao, Chenchen Zhu, Xiaoliang Dai, Dilin Wang, Fei Sun, Forrest Iandola, et al. Efficientsam: Leveraged masked image pretraining for efficient segment anything. In *Proceedings of the IEEE/CVF Conference on Computer Vision and Pattern Recognition*, pages 16111–16121, 2024. [2](#)
- [30] Chaoning Zhang, Dongshen Han, Yu Qiao, Jung Uk Kim, Sung-Ho Bae, Seungkyu Lee, and Choong Seon Hong. Faster segment anything: Towards lightweight sam for mobile applications. *arXiv preprint arXiv:2306.14289*, 2023. [2](#)
- [31] Shuaifeng Zhi, Tristan Laidlow, Stefan Leutenegger, and Andrew J Davison. In-place scene labelling and understanding with implicit scene representation. In *Proceedings of the IEEE/CVF International Conference on Computer Vision*, pages 15838–15847, 2021. [2](#)
- [32] Jiayuan Zhu, Abdullah Hamdi, Yunli Qi, Yueming Jin, and Junde Wu. Medical sam 2: Segment medical images as video via segment anything model 2. *arXiv preprint arXiv:2408.00874*, 2024. [2](#)